The Astrophysical Journal, 849:130 (13pp), 2017 November 10 https://doi.org/10.3847/1538-4357/aa9227

Gas Mass Tracers in Protoplanetary Disks: CO is Still the Best

Tamara Molyarova[1,2], Vitaly Akimkin[1], Dmitry Semenov[3], Thomas Henning[3], Anton Vasyunin[4,5], and Dmitri Wiebe[1]
[1] Institute of Astronomy, Russian Academy of Sciences, 48 Pyatnitskaya St., Moscow, 119017, Russia; molyarova@inasan.ru
[2] Moscow Institute of Physics and Technology (State University), 9 Institutskiy per., Dolgoprudny, Moscow Region, 141700, Russia
[3] Max Planck Institute for Astronomy, Königstuhl 17, D-69117 Heidelberg, Germany
[4] Max Planck Institute for Extraterrestrial Physics, Giessenbachstrasse, D-85748 Garching, Germany
[5] Ural Federal University, Ekaterinburg, 620083, Russia
Received 2017 June 14; revised 2017 October 6; accepted 2017 October 7; published 2017 November 8

Abstract

Protoplanetary disk mass is a key parameter controlling the process of planetary system formation. CO molecular emission is often used as a tracer of gas mass in the disk. In this study, we consider the ability of CO to trace the gas mass over a wide range of disk structural parameters, and we search for chemical species that could possibly be used as alternative mass tracers to CO. Specifically, we apply detailed astrochemical modeling to a large set of models of protoplanetary disks around low-mass stars to select molecules with abundances correlated with the disk mass and being relatively insensitive to other disk properties. We do not consider sophisticated dust evolution models, restricting ourselves to the standard astrochemical assumption of 0.1 μm dust. We find that CO is indeed the best molecular tracer for total gas mass, despite the fact that it is not the main carbon carrier, provided reasonable assumptions about CO abundance in the disk are used. Typically, chemical reprocessing lowers the abundance of CO by a factor of 3, compared to the case where photodissociation and freeze-out are the only ways of CO depletion. On average, only 13% C atoms reside in gas-phase CO, albeit with variations from 2% to 30%. CO_2, H_2O, and H_2CO can potentially serve as alternative mass tracers, with the latter two only applicable if disk structural parameters are known.

Key words: astrochemistry – circumstellar matter – protoplanetary disks

1. Introduction

A young Sun-like star at its early evolutionary stage is generally surrounded by a flattened rotating gas and dust structure, which is commonly referred to as a protoplanetary disk even though evidence of planet formation in these disks is still mostly circumstantial (see, e.g., reviews by Williams & Cieza 2011; Armitage 2015). Although the exact scenario of planet formation remains debated, the mass of the protoplanetary disk is thought to play a key role in this process (Mordasini et al. 2012; Bitsch et al. 2015). Therefore, estimating accurate disk masses from observations is one of the most important but also most challenging tasks in studies of formation and early evolution of planetary systems.

There are two different approaches to measuring disk masses. The most common way is to observe the dust continuum emission. Provided this emission is optically thin (which is expected at submillimeter and millimeter wavelengths), one can calculate the total dust mass in the disk (Andrews & Williams 2005; Williams & Cieza 2011) from the integrated continuum flux. Then, to convert the dust mass into total disk mass, the standard interstellar gas-to-dust ratio of 100 can be adopted (Bohlin et al. 1978). However, to apply this method, one needs to know the dust temperature in the disk, because the same flux at a given wavelength may come from both a larger amount of cold dust or a smaller amount of warm dust. Such a mass derivation requires assumptions about dust optical properties, which are not well-constrained for dust grains in protoplanetary disks and also may change as dust grows at early stages of planet formation (Draine 2006; Henning & Meeus 2011). Furthermore, it is far from obvious that the interstellar gas-to-dust mass ratio is valid for protoplanetary disks. Dunham et al. (2014) and Tsukamoto et al. (2017) suggest that masses of young disks derived from dust observations may be underestimated.

The more direct way to measure gas mass in disks is to observe molecular emission lines. Although disks mostly consist of molecular hydrogen and helium, these components either cannot be observed directly or trace only a limited disk region (see, e.g., Carmona et al. 2011), and other mass tracers are commonly employed, which require knowledge of a conversion factor from tracer mass to H_2 mass. In this respect, hydrogen deuteride (HD) seems to be a good candidate (Bergin et al. 2013; McClure et al. 2016) as it is well coupled to molecular hydrogen and also has a relatively high abundance of $3 \cdot 10^{-5}$ relative to H_2, although using it as a mass tracer may lead to a factor of 3 uncertainty (Trapman et al. 2017). Currently, the only facility that will be able to produce new HD measurements will be SOFIA with its forthcoming HIRMES spectrograph.

A widely used molecular mass tracer in disks is carbon monoxide (CO), as it is one of the most abundant species in interstellar and circumstellar material and possesses rotational transitions that are easy to observe. Hydrogen mass determination using CO lines is usually applied to diffuse clouds (Goldsmith et al. 1997; Bolatto et al. 2013), but now it is also commonly used for protoplanetary disks (Williams & Best 2014; Ansdell et al. 2016; Miotello et al. 2016; Williams & McPartland 2016). However, the CO-based disk mass determination method has some recognized problems, too. First, CO emission is optically thick, which can be circumvented by observing CO isotopologues ^{13}CO, $C^{18}O$, $C^{17}O$, and also $^{13}C^{18}O$, which has been recently observed in the TW Hya disk (Zhang et al. 2017). Their lines are typically optically thin as they are less abundant (Qi et al. 2011). The second problem is that CO, along with its isotopologues,

freezes out in cold dense regions of the disk midplane and becomes non-observable (Henning & Semenov 2013).

Given the lack of good alternatives, CO observations are still vital for the determination of protoplanetary disk mass. However, its application for that purpose should be validated with theoretical models that include both radiation transfer (RT) and chemistry. Williams & Best (2014) constructed a model of CO distribution over a selection of parameterized protoplanetary disks, assuming that CO is frozen in those regions of the disk where the temperature is below 20 K and is photodissociated above the vertical H_2 column density of $1.3 \times 10^{21}\,\mathrm{cm}^{-2}$. In the remaining part of the disk, the CO abundance relative to H_2 was assumed to be equal to the so-called "interstellar" value, 10^{-4} (France et al. 2014). Williams & Best (2014) pointed out that under these assumptions, CO mass in this warm molecular zone represents a significant fraction of the total CO mass and thus traces the bulk of the disk gas mass. However, the CO-based disk gas masses derived so far seem to be systematically smaller than the masses derived from dust observations. ALMA disk surveys in Lupus, Chamaeleon, σ Orionis, and other star-forming regions by Ansdell et al. (2016, 2017) based on the same theoretical model suggest very high dust-to-gas mass ratios up to 1/10.

Williams & Best (2014) suggested that the difference between the CO-based disk mass and the dust-based disk mass can be both real (reflecting low gas-to-dust mass ratios) and related to an uncertainty in the CO-to-H_2 abundance ratio, if, for example, some other CO depletion pathways are more efficient. This possibility was explored by Miotello et al. (2016) with the isotope-selective chemical model by means of artificially reduced carbon abundance. However, they only considered simple hydrogenation surface processes, which may somewhat decrease gas-phase CO abundance. They noted that the uncertainty in the CO-based gas mass estimate can be reduced if some information on the disk structure is available. A continuation of this study was presented by Miotello et al. (2017), who confirmed that simplified surface chemistry may be the cause of discrepancy of disk masses estimated using CO and dust observations.

A more detailed surface chemistry model was utilized in the work of Yu et al. (2016). These authors considered CO evolution in the model of an accretion-heated disk and found that even inside a CO snowline, gas-phase CO abundance can be reduced significantly due to the conversion of CO into other less volatile species, like CO_2 and complex organic molecules, which is a common effect at various stages of star formation (Vasyunina et al. 2012). However, only a limited number of disk models was considered in this study, and only the inner part of the disk (within 70 au) was analyzed. Also, Yu et al. (2016) assumed that significant dust evolution has already taken place in the disks, so that most dust grains have coagulated into larger particles, limiting the efficiency of both CO freeze-out and surface conversion into other molecules. Yu et al. (2017) extended this study and came to the conclusion that the chemical depletion of CO may lead to a significant underestimation of the disk gas masses.

In this study, we intend to combine a large grid of disk physical models with a comprehensive chemical model, which includes a detailed treatment of surface chemistry. We check the degree of reliability of CO as a gas mass tracer with realistic variations of the disk parameters and the uncertainties related to CO chemical depletion. We perform an analysis of the carbon partition into gas and solid species. The computed set of models is used to look for other possible tracers of disk gas mass.

2. Model

The basis for our study is a set of ~1000 disk models (described in detail in Section 2.3), which allows the distribution of gas-phase and surface molecular abundances for a selection of disk structural parameters to be studied. We utilize a modified version of the ANDES code (Akimkin et al. 2013) combined with the updated ALCHEMIC network (Semenov & Wiebe 2011) to follow the evolution of molecular abundances.

2.1. Physical Structure

For the parameterization of the disk surface density, we adopt the commonly used tapered power-law profile (Hartmann et al. 1998)

$$\Sigma(R) = \Sigma_0 \left(\frac{R}{R_c}\right)^{-\gamma} e^{-(R/R_c)^{2-\gamma}}, \quad (1)$$

where Σ_0 in $\mathrm{g\,cm}^{-2}$ is the surface density normalization, γ parameterizes the radial dependence of the disk viscosity, and R_c is a characteristic radius of the disk. Σ_0 can be calculated from the total disk mass as

$$\Sigma_0 = \frac{M_{\mathrm{disk}}(2-\gamma)}{2\pi R_c^2}. \quad (2)$$

So, the surface density radial profile depends on three parameters: M_{disk}, γ, and R_c.

We assume that the disk is axially symmetric and its vertical structure at each radius is determined by the hydrostatic equilibrium

$$\frac{\partial P(R,z)}{\partial z} = -\rho(R,z)\frac{zGM_\star}{(R^2+z^2)^{3/2}}, \quad (3)$$

$$P = \frac{k_B T(R,z)}{\mu m_p}\rho(R,z), \quad (4)$$

where the disk temperature distribution $T(R, z)$ is calculated using a simple parameterization (Williams & Best 2014; Isella et al. 2016),

$$T(R,z) = \begin{cases} T_a(R, z=z_q) + [T_m(R) - T_a(R, z=z_q)]\left(\cos\dfrac{\pi z}{2z_q(R)}\right)^2, & \text{if } |z| < z_q(R), \\ T_a(R,z), & \text{if } |z| \geqslant z_q(R). \end{cases} \quad (5)$$

Rather than adding the disk atmosphere and midplane temperatures $T_{\rm m}$ and $T_{\rm a}$ to our set of parameters, we calculate them at the base of the central luminosity source (star plus accretion region). The optically thin disk atmosphere can be easily ray-traced as dust thermal radiation does not contribute significantly to the source function. The dust temperature is determined from the thermal balance equation,

$$\int_0^\infty \kappa_\nu J_\nu d\nu = \int_0^\infty \kappa_\nu B_\nu(T_{\rm a}) d\nu, \quad (6)$$

where κ_ν in cm^{-1} is the dust absorption coefficient and J_ν is the mean intensity of the radiation coming directly from the central star, accretion region, and interstellar medium,

$$J_\nu = J_{\nu,{\rm s}} + J_{\nu,{\rm acc}} + J_{\nu,{\rm ISRF}} = W_\star B_\nu(T_\star) e^{-\tau_{\nu,1}} + W_{\rm acc} B_\nu(T_{\rm acc}) e^{-\tau_{\nu,1}} + \frac{1}{3} I_{\rm ISRF}(e^{-\tau_{\nu,2}} + e^{-\tau_{\nu,3}} + e^{-\tau_{\nu,4}}). \quad (7)$$

Here, $W_\star = \frac{1}{4}R_\star^2/(R^2+z^2)$ and $W_{\rm acc} = \frac{1}{4}R_{\rm acc}^2/(R^2+z^2)$ represent the dilution factors for the radiation from the central star and accretion region, and $R_\star$ and $T_\star$ are the stellar radius and effective temperature. The accretion luminosity is simulated by the additional central source of irradiation with effective radius $R_{\rm acc}$ and effective temperature $T_{\rm acc}$, so that $L_{\rm acc} = 4\pi R_{\rm acc}^2 \sigma_{\rm SB} T_{\rm acc}^4 = (3/2) G M_\star \dot{M}/R_\star$. We assume a typical accretion rate of $\dot{M} = 10^{-8}\,M_\odot$ yr^{-1} and $T_{\rm acc} = 15{,}000$ K to calculate the effective radius of an accretion region, $R_{\rm acc}$. The interstellar radiation field is adopted from Mathis et al. (1983).

The optical depth in Equation (7), $\tau_{\nu,k} = \int(\kappa_\nu + \sigma_\nu) dl$, is calculated along four directions: to and from the star ($k = 1, 2$), and up and down ($k = 3,\ 4$). Dust optical properties are computed from the Mie theory for astrosilicate grains (Laor & Draine 1993) assuming a dust-to-gas ratio of 0.01. We use a spatial grid R_n and z_{nm} such that z_{nm}/R_n is constant for a given m. This greatly reduces the computational cost for the ray-tracing procedure as all spatial points with a fixed $m$index are located on the same line.

We define $z_{\rm q}(R)$ as the height at which $T_{\rm a}$ has a maximum at a given R. Above $z_{\rm q}(R)$, the dust temperature decreases with z due to increasing distance from the star; the drop in temperature below $z_{\rm q}(R)$ is explained by the absorption. This also means that the source function starts to be dominated by the dust thermal infrared radiation and not by the radiation from the star. In this regime, the approximation for radiation intensity (7) is no longer valid. The temperature profile below $z_{\rm q}(R)$ is set according to Equation (5), with the midplane temperature adopted from the optically thick case of the two-layered model (Chiang & Goldreich 1997; Dullemond et al. 2001),

$$T_{\rm m}^4(R) = \frac{1}{2}\varphi\left[T_\star^4\left(\frac{R_\star}{R}\right)^2 + T_{\rm acc}^4\left(\frac{R_{\rm acc}}{R}\right)^2\right], \quad (8)$$

where $\varphi = 0.05$ is a flaring angle (Dullemond & Dominik 2004), and the factor $\frac{1}{2}$ reflects the fact that only half of the infrared radiation from the super-heated upper layer of the disk heats the midplane and the other half is emitted outward. This midplane temperature differs from the disk effective temperature by a factor of $\sqrt[4]{2}$. Gas and dust temperatures are assumed to be equal. We use iterations to obtain self-consistent density and temperature structures, which is important for the ray-tracing procedure and calculation of the atmosphere temperature. However, in the calculation of the midplane temperature, we keep the flaring angle fixed to avoid disk self-shadowing as this effect must be studied by means of a more sophisticated model. The adopted model for the disk physical structure enables us to perform astrochemical simulations for a large set of models while keeping the adequate level of accuracy.

The values of the stellar radius $R_\star$, effective temperature $T_\star$, and stellar mass $M_\star$ used in the above parameterizations are not independent. We take $M_\star$ as a primary parameter and calculate $R_\star$ and $T_\star$ from the evolutionary tracks of Baraffe et al. (2015), assuming a stellar age of 3 Myr. As their model is restricted to low-mass stars, we only consider T Tauri-type stars with masses between 0.5 and 1.4 $M_\odot$. Stellar and accretion luminosities are assumed to be constant during the chemical run. However, luminosity bursts may have a lasting impact on the disk chemical structure and are a topic of current research (Harsono et al. 2015; Rab et al. 2017).

Overall, we have four parameters, $M_{\rm disk}$, γ, $R_{\rm c}$, and $M_\star$, that determine the physical structure of the disk. The spatial grid has 50 points in the radial direction between 1 and 1000 au, and 80 points in the vertical direction from the midplane to $z/R = 0.5$.

2.2. Chemical Model

The chemical structure is calculated with the modified version of the thermochemical non-equilibrium ANDES code (Akimkin et al. 2013). The system of chemical kinetics equations was updated to account for the gas–grain chemistry of the ALCHEMIC model (Semenov & Wiebe 2011). The gas-phase part was benchmarked with the NAHOON code (Wakelam et al. 2015), which resulted in fixing several non-critical bugs. Some rate coefficients were updated in accordance with the KIDA14 database. Overall, the chemical network contains 650 species involved in 7807 reactions. No isotope-selective chemistry is considered.

The original version of the ANDES code contains a module to calculate the thermal balance of gas and dust. We replaced this module in the current study by a phenomenological setup for the thermal structure in order to reduce computational costs for modeling a large set of disks. However, the 2D RT of UV radiation was implemented in order to calculate photoreaction rates. The RT is based on the short characteristics method and allows for the radiation field calculation up to optical depths $\tau_{\rm UV} \sim 10$. The MRN grain size distribution (Mathis et al. 1977) and dust-to-gas ratio of 0.01 are taken as the dust model for the RT modeling in the disk atmosphere. We calculate RT for the stellar and interstellar radiation field and also consider X-rays, cosmic rays (CR), and radioactive nuclides as sources of ionization. The spectrum of a central star is assumed to be a blackbody with an effective temperature corresponding to a given stellar mass plus a UV excess produced by accretion (as stated above). Although the real stellar spectra may not be well-represented by a blackbody, in the context of our study, only the relation between the visible and far-UV spectrum parts is important. The X-ray ionization rate is calculated on the basis of the Bai & Goodman (2009) model (their Equation (21)), assuming X-ray luminosity $L_{\rm X} = 10^{30}$ erg s^{-1} and $T_{\rm X} = 3$ keV. We use $\zeta_0 = 1.3 \times 10^{-17}$ s^{-1} for the unattenuated cosmic-ray ionization rate and an attenuation length of 96 g cm^{-2} (Sano

Table 1
Initial Abundances (Relative to H Nuclei)

Species	H_2	H	He	C^+	N	O	S^+
Abundance	0.499	0.002	0.09	$7.3 \cdot 10^{-5}$	$2.14 \cdot 10^{-5}$	$1.76 \cdot 10^{-4}$	$8 \cdot 10^{-8}$
Species	Si^+	Fe^+	Na^+	Mg^+	P^+	Cl^+	...
Abundance	$8 \cdot 10^{-9}$	$3 \cdot 10^{-9}$	$2 \cdot 10^{-9}$	$7 \cdot 10^{-9}$	$2 \cdot 10^{-10}$	$1 \cdot 10^{-9}$	...

et al. 2000) and $\zeta_{RA} = 6.5 \times 10^{-19}\,s^{-1}$ for the ionization rate by radioactive elements.

The initial abundances are presented in Table 1 and correspond to the "low-metals" case of Lee et al. (1998), unless otherwise noted.

Apart from gas-phase processes, our chemical network includes surface reactions along with accretion and desorption. As many species tend to freeze out onto dust particles, which makes them unobservable, surface chemistry is crucial for such models. We adopt the ratio of diffusion energy to desorption energy of 0.5 and account for tunneling through reaction barriers. Single-layer surface chemistry is considered. Our treatment of surface chemistry includes reactive desorption with an efficiency of 1%, which means that in two-body surface reactions, 99% of the product species stay on the surface and 1% is released into gas, although a more detailed treatment of reactive desorption is already available in some astrochemical models (Vasyunin et al. 2017). The representative size of dust grains in the grain chemistry treatment is assumed to be 0.1 μm. In protoplanetary disks, dust is supposed to grow, which reduces the available dust surface and slows down the surface chemistry. Also, grown dust makes the disk more transparent to stellar radiation. However, the theoretical description of dust evolution is a complicated task, especially when taking into account such poorly studied effects such as grain charging (Okuzumi 2009; Akimkin 2015; Ivlev et al. 2016). Therefore, we ignore dust evolution effects and focus on varying the disk macrophysical parameters.

2.3. Set of Models

Like Williams & Best (2014), we create a grid of models with variable parameters responsible for the disk's physical structure. As we already mentioned, these parameters are the disk mass M_{disk}, stellar mass $M_\star$, effective radius of the disk R_c, and power-law index γ. We vary them within bounds typical for protoplanetary disks around T Tauri stars. Specific ranges for each parameter are presented in Table 2.

We calculate the 2D distributions of 650 species for time moments of 0.5, 1, and 3 Myr, and use these distributions to compute the total species masses in the disk. In Section 3.1, we employ a random set of models, with every parameter being uniformly distributed inside the ranges (for the disk mass, it is $\log_{10} M_{disk}$ that is distributed uniformly). In Section 3.3, we use a grid of models with fixed nodes and present various cuts through the parameter space.

Table 2
Range of Parameters Used in the Set of Models

Parameter	Value
M_{disk}	$10^{-4} \div 10^{-1}\,M_\odot$
$M_\star$	$0.5 \div 1.4\,M_\odot$
R_c	$30 \div 200$ au
γ	$0.5 \div 1.5$

3. Results

3.1. Potential Gas Mass Tracers

The list of molecules observed in protoplanetary disks is currently not very extensive and includes CN, HCN, HNC, CS, SO, H_2CO, CCH, HC_3N, CH_3CN, C_3H_2, C_2H_2, OH, HCO^+, N_2H^+, CH^+, C^+, O, NH_3, and CH_3OH (Dutrey et al. 1997, 2011; Thi et al. 2011; Chapillon et al. 2012; Qi et al. 2013; Öberg et al. 2015; Guilloteau et al. 2016; Salinas et al. 2016; Walsh et al. 2016). It would be interesting to find out if some of them could possibly serve as a gas mass tracer alternative to commonly used CO. Also, pending future discoveries of molecules in protoplanetary disks, we do not exclude from consideration other chemical species present in the model.

The total disk abundance of a prospective disk mass tracer $X_i = N_i / N_{\langle H \rangle}$ should be correlated with the disk mass, while being less dependent on other physical properties of the disk, such as the density profile, disk radius, or properties of the central star. The correlation should not necessarily be linear, implying the independence of the total abundance from the disk mass. In principle, the species abundance can be any monotonic function of the disk mass. Also, it should not vary significantly with time.

To assess the potential applicability of the species as a disk mass tracer, we need to introduce some quantitative gauges. For every jth disk model in the ensemble, we calculate the total logarithmic abundance of the ith species, $x_{ij} = \log_{10}(X_{ij})$. The value $\overline{x_i}$, averaged over the disk model ensemble, represents a typical (logarithm of) total disk abundance of the ith species. We employ its dispersion $s_i^2 = \overline{(x_{ij} - \overline{x_i})^2}$ as a simple quantitative measure of suitability of the ith species as a mass tracer. Further, we refer to the standard deviation s_i as a "scatter parameter" to stress the limitation of the approach. First, the distribution of the protoplanetary disk parameters is not well-known and quite probably differs from the uniform distribution assumed during the disk ensemble generation. Second, the scatter may not reflect the nonlinear scaling between the disk and species mass. However, generally speaking, the smaller the scatter, the better the species performs as a mass tracer.

Table 3 summarizes this simple statistical analysis and contains the total disk abundances and scatter parameters for the model age of 3 Myr, sorted by increasing s_i. For other chemical ages, the values of the scatter parameter are about the same, slightly growing with time. We include components with average total disk abundance greater than 10^{-11}, excluding ices and common species like H_2 and He. All of the detected species listed above are present in the table as well. The species that are potentially observable with *JWST* but not with ALMA are marked with a star (*). Total disk abundances for ice species are given in the Appendix in the table analogous to Table 3.

Table 3
Average Total Disk Abundance $\overline{X_i} = 10^{\overline{x_i}}$ and Scatter s_i for Selected Species

Species	$\overline{X_i}$	s_i (dex)	Species	$\overline{X_i}$	s_i (dex)	Species	$\overline{X_i}$	s_i (dex)
N_2	2.0×10^{-6}	0.25	C_6	1.5×10^{-11}	0.45	C	4.9×10^{-6}	0.64
NH_3	3.2×10^{-9}	0.27	HCN	2.4×10^{-9}	0.45	O_3	5.5×10^{-8}	0.64
CH_3	3.6×10^{-10}	0.28	Si	1.7×10^{-10}	0.46	O	2.1×10^{-5}	0.66
CO	8.0×10^{-6}	0.28	C_4H	1.0×10^{-10}	0.46	C_2H_6	2.3×10^{-9}	0.66
H_3^+	2.2×10^{-10}	0.28	$^*C_2H_2$	4.3×10^{-10}	0.47	CH_3^+	3.8×10^{-11}	0.73
$^*CO_2$	5.2×10^{-7}	0.28	Na	1.9×10^{-10}	0.48	C_2H	6.6×10^{-10}	0.74
H_2CO	1.3×10^{-10}	0.29	N_2H^+	1.3×10^{-11}	0.48	Na^+	1.8×10^{-10}	0.74
H_3O^+	2.6×10^{-10}	0.30	CS	4.7×10^{-10}	0.49	N	1.5×10^{-6}	0.75
H_2CN^+	1.6×10^{-11}	0.31	Mg	4.0×10^{-11}	0.49	H_5C_3N	2.2×10^{-11}	0.77
H_2CS	1.6×10^{-11}	0.32	H_2C_3O	4.7×10^{-10}	0.50	CH_2	5.6×10^{-10}	0.77
NH_2	3.5×10^{-10}	0.32	MgH_2	5.2×10^{-10}	0.50	HC_2O	6.9×10^{-11}	0.80
SO_2	2.1×10^{-10}	0.32	HS	2.1×10^{-10}	0.51	N_2O	1.2×10^{-10}	0.81
HNO	1.4×10^{-10}	0.33	CH_2CO	1.8×10^{-10}	0.51	S^+	4.9×10^{-9}	0.81
C_3	1.3×10^{-8}	0.34	CH_5N	2.5×10^{-11}	0.51	HCCN	5.0×10^{-11}	0.81
C_5H_3	2.5×10^{-11}	0.35	$^*H_2O$	4.0×10^{-7}	0.51	P^+	1.1×10^{-11}	0.82
SO	2.7×10^{-9}	0.37	Cl	1.8×10^{-10}	0.51	Si^+	5.1×10^{-10}	0.83
C_3H	1.1×10^{-10}	0.39	CH_3CN	2.0×10^{-11}	0.52	CH	1.5×10^{-9}	0.83
OCN	1.7×10^{-10}	0.40	HNC	1.2×10^{-9}	0.52	Fe^+	1.6×10^{-10}	0.84
$^*OH$	1.4×10^{-8}	0.41	H_2O_2	4.0×10^{-9}	0.53	Mg^+	3.3×10^{-10}	0.84
P	1.5×10^{-11}	0.41	C_4H_2	2.4×10^{-11}	0.53	O_2H	1.3×10^{-11}	0.85
HC_3O	3.2×10^{-11}	0.41	C_2H_4	1.7×10^{-11}	0.54	CN	1.4×10^{-9}	0.86
H_2S	1.3×10^{-9}	0.41	C_5	1.1×10^{-10}	0.54	HC_3N	1.6×10^{-11}	0.86
FeH	2.4×10^{-10}	0.42	C_3H_2	8.7×10^{-11}	0.54	C^+	1.5×10^{-6}	0.88
C_4	1.6×10^{-10}	0.43	C_5H_2	2.1×10^{-11}	0.55	C_9H_2	2.3×10^{-11}	0.94
NO	4.1×10^{-9}	0.43	$^*CH_4$	7.7×10^{-8}	0.55	C_5H_4	2.9×10^{-11}	0.97
NH	9.6×10^{-11}	0.43	CH_3OH	9.3×10^{-11}	0.56	C_2	1.2×10^{-9}	1.02
S	6.5×10^{-9}	0.43	C_5H	2.2×10^{-11}	0.57	CH_2NH_2	4.8×10^{-11}	1.09
SiO	3.4×10^{-10}	0.43	CH_2OH	4.1×10^{-11}	0.59	CH_3NH	4.7×10^{-11}	1.09
$^*O_2$	2.4×10^{-6}	0.44	HCO^+	8.7×10^{-11}	0.60	CH^+	3.7×10^{-13}	1.19
HNCO	1.9×10^{-9}	0.44	HCOOH	1.3×10^{-11}	0.63	N_2H_2	6.9×10^{-11}	1.22

The top of the table is occupied by N_2, NH_3, CH_3, CO, H_3^+, and CO_2, and in Figure 1, their total masses are shown as functions of the total disk mass. In each panel, a solid line is shown with the slope corresponding to the linear scaling of the species mass with the disk mass at the average total abundance $\overline{X_i} = 10^{\overline{x_i}}$ from Table 3. A scatter parameter is also indicated in each panel. Molecular nitrogen seems to be the best theoretical mass tracer as its mass scales almost linearly with the disk mass over the entire range of considered disk masses. This molecule, like H_2, has no rotational transitions and thus cannot be observed directly, but $^{14}N\,^{15}N$ has such transitions. Despite the fact that the mass difference between ^{14}N and ^{15}N is small and hence the dipole moment is very weak, theoretically, one could detect its fundamental rotational line at 4.34 μm in disks.

The CO total mass also shows nearly linear scaling with the disk mass, but with a scatter that increases somewhat in more massive disks. Disks with lower γ values (shallower density profiles) tend to have smaller CO abundance, while more compact disks (with lower γ and R_c, i.e., smaller and redder dots in Figure 1) are more CO rich. The reason is that in a compact disk, most mass is located in a warm disk area, where CO freeze-out is prohibited. As we consider larger and/or shallower disks, more mass is shifted to colder disk areas.

The dashed line in the top-left panel of Figure 1 indicates the maximum possible CO mass, corresponding to the assumption that all carbon atoms are locked in gas-phase CO. In this extreme case, $M_{CO} = 1.5 \times 10^{-3} M_{disk}$. According to our results, the computed total CO mass is much lower in all of the considered models, and its typical value is only $1.7 \times 10^{-4} M_{disk}$. Most carbon atoms are locked up not in CO but in CO_2 ice. Carbon redistribution is discussed in more detail in Section 3.2.

The scatter parameters for NH_3 and CH_3 are formally somewhat lower than the one for CO. However, inspection of Figure 1 shows that the masses of these species depend more strongly on the disk structure than on the CO mass, if the disk mass exceeds $\sim 10^{-3} M_\odot$. Also, ammonia masses lose the linear scaling with disk masses in the least massive disks. Additionally, abundances of NH_3 and CH_3, as well as that of H_3^+, are quite low, which hampers their detection. While NH_3 has nevertheless been detected by *Herschel* in the nearby TW Hya disk (Salinas et al. 2016), the methyl radical and H_3^+ have no allowed dipole moment as they are symmetric and planar. Potentially, H_3^+ can be traced by o-H_2D^+; thus, even though we do not consider isotopic chemistry, o-H_2D^+ may also correlate well with the disk gas mass. However, detecting this species in disks is challenging even for ALMA (Chapillon et al. 2011).

Carbon dioxide looks quite promising. Its scatter only slightly exceeds that of CO, and it will also be observable by *JWST*. Although the dependence of its mass on the disk mass is nonlinear in disks with the lowest masses, this is compensated by uniformly low scatter and linear scaling for disks with masses above $\sim 10^{-3} M_\odot$.

Overall, we conclude that CO is currently the best mass tracer, combining ease of detection and predictability of behavior. Among other species, some are better than others, with the scatter comparable to that of CO (see Figure 2). Water mass scales with the disk mass for $M_{disk} > 10^{-3} M_\odot$, but in the least massive disks, the water abundance shows a significant

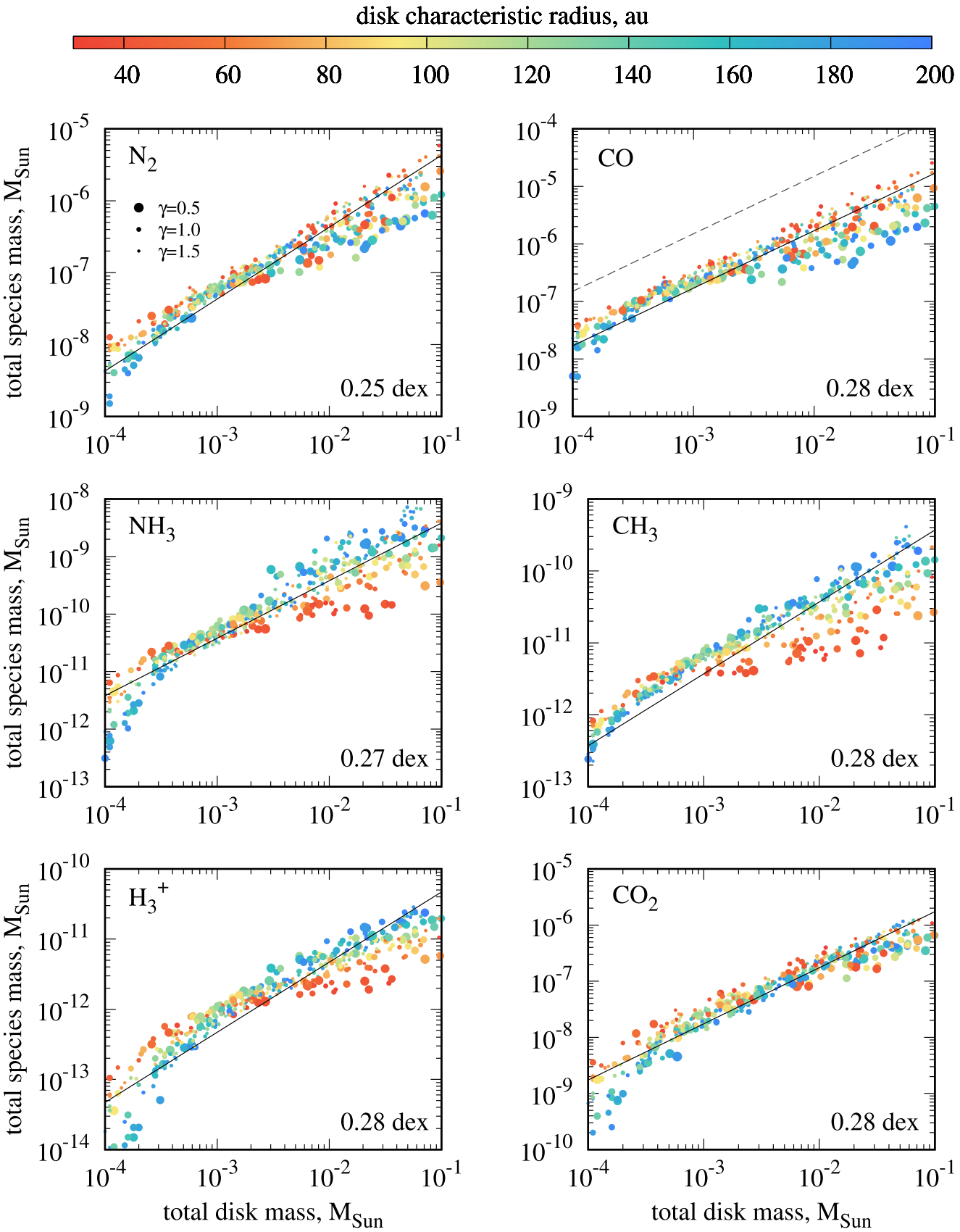

Figure 1. Total mass of species with the lowest scatter values in the disk as a function of the disk mass at an age of 3 Myr. The point size depicts the γ value (larger symbols represent shallower surface density profiles), the point color represents the disk characteristic radius R_c. The solid lines indicate linear scaling, with the slope equal to the average mass fraction. The dashed line corresponds to the CO amount if it were to contain all of the available carbon atoms. The scatter parameter is shown in the bottom-right corner of each panel.

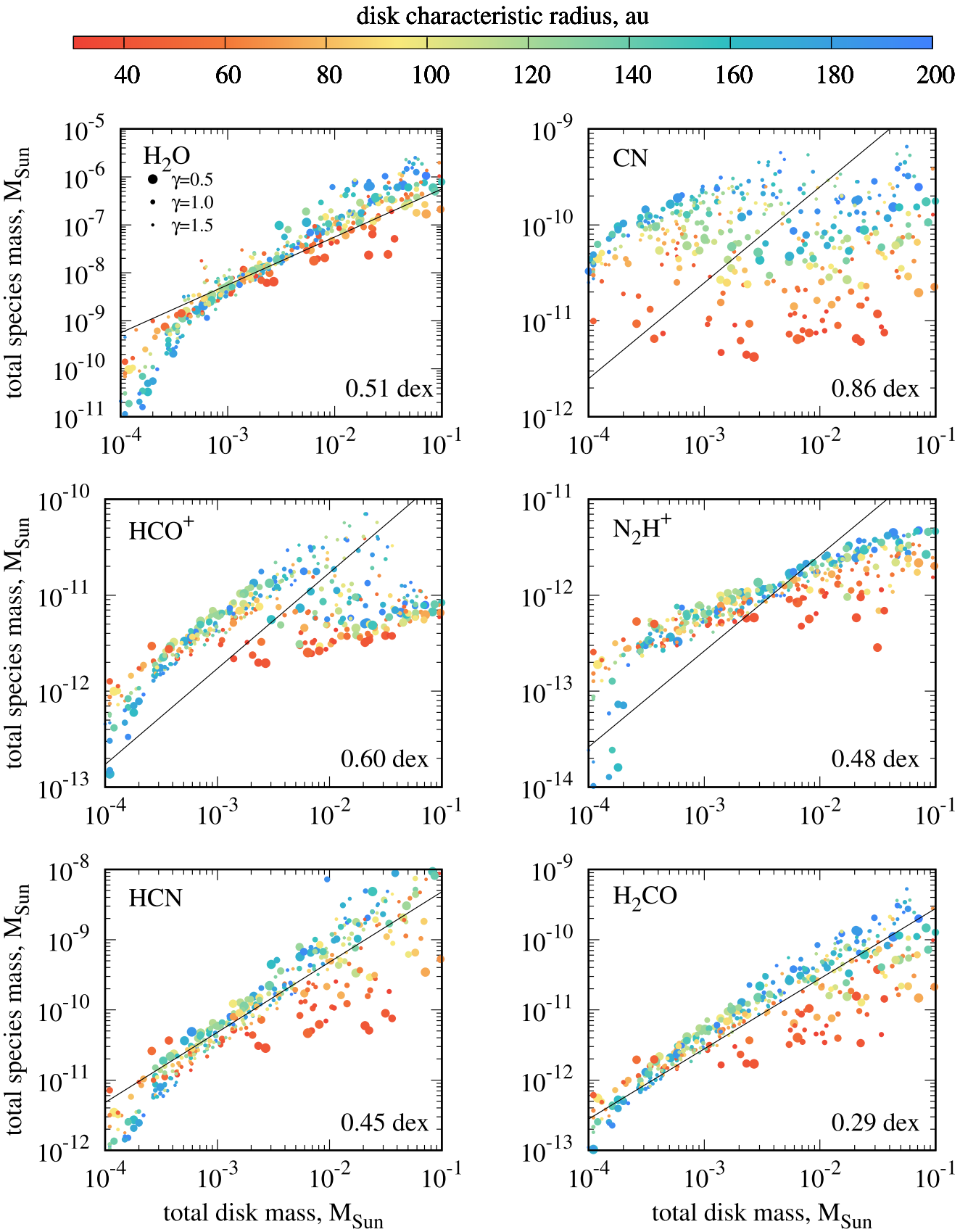

Figure 2. Same as in Figure 1, but for species with higher scatter values.

scatter (of about two orders of magnitude), with smaller γ values and more extended disks corresponding to lower water masses. This seems to be interesting in view of the diverse results of *Herschel* water observations in the disks of DM Tau (Bergin et al. 2010) and TW Hya (Hogerheijde et al. 2011). Quite different water abundances

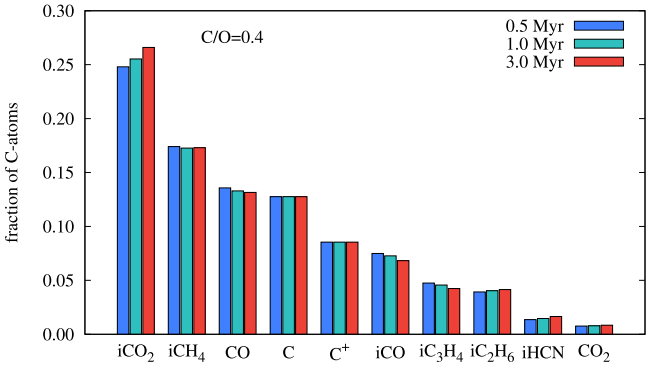

Figure 3. Distribution of carbon between major carbon-bearing molecules for different disk ages, averaged over the models. Ice species are denoted by a leading "i." C/O = 0.4 is the ratio of carbon to oxygen elemental abundances.

may reflect not only evolutionary changes but also structural variations.

Other carbon-bearing species show a significant scatter across the entire disk mass range, and the scatter generally increases as the disk mass increases. But in some cases, the uncertainty can be reduced significantly if the disk size is known. Intriguingly, the H_2CO emission detected in disks could potentially be used as a proxy of disk mass, since the H_2CO disk mass factor has a low scatter similar to CO and is quite tight (albeit nonlinear), if most compact disks are excluded. On the other hand, the H_2CO emission in disks shows a peculiar ring-like structure (Henning & Semenov 2008; Loomis et al. 2015; Öberg et al. 2017), which makes such an analysis a difficult endeavor. The CN and HCO^+ scaling are sufficiently nonlinear, which hampers their use as mass tracers.

An interesting case is represented by N_2H^+. The dependence of its mass on the disk mass is quite tight over the entire $M_{\rm disk}$ range and shows extreme sensitivity to the disk mass for $M_{\rm disk} < 3 \times 10^{-4}\,M_\odot$. However, at higher $M_{\rm disk}$ values, the dependence of N_2H^+ mass on the disk mass is much weaker. This should be related to CO behavior. In extremely low-mass disks, CO is depleted from the gas phase only due to freeze-out. In more massive disks, CO also experiences chemical depletion due to carbon redistribution into other species. The steeper left part of the N_2H^+ graph (see Figure 2) reflects the developing chemical depletion of CO, while at the shallower right part, this process is saturated. The change of N_2H^+ abundance in more massive disks is explained by the shift of N_2H^+ from the midplane to the upper layers.

3.2. Carbon Redistribution

In this section, we consider major carbon-bearing species and demonstrate that gaseous CO is not the main reservoir of carbon in the considered protoplanetary disks. For each disk, we find molecules that are major carbon reservoirs and calculate what percentage of carbon they comprise. The distribution of carbon among the top 10 carbon-bearing species is plotted in Figure 3. Three time moments are presented, 0.5, 1, and 3 Myr, showing that this distribution does not change much with the disk age.

There are two reasons for such a behavior. First, we show the carbon fraction integrated over the entire disk, and most of material contributing to this value is relatively warm and dense, allowing chemical equilibrium to be reached within 0.5 Myr. Second, the ice species shown are relatively simple, and their formation does not involve long-scale surface chemistry, so that they also have short typical chemical timescales.

We do see, however, some temporal changes in the carbon fraction for some species. The fraction of CO_2 ice gradually increases with time, while fractions of CO in gas and ice diminish mostly due to the conversion of iCO into iCO_2 on the dust surfaces. Other molecule fractions also demonstrate some trends, so the redistribution of carbon in disks slowly continues during the considered time.

The diagram in Figure 3 shows that carbon is mostly locked in CO_2 ice ($27\% \pm 8\%$) at 3 Myr, but a sufficient fraction of carbon stays in the elementary forms of C or C^+. Among the 10 major carbon-bearing molecules, which constitute 95% of all available C atoms, only four are in the gas phase. The most abundant gas-phase species is CO with an average of 13%, while gas-phase CO_2 comprises only about 1%. In other words, only every seventh C atom belongs to CO in a gas form. The prevalence of CO_2 ice, which is mostly formed on grains, stresses the necessity of proper surface chemistry treatment.

In Figure 4, we present the distribution of important C-containing molecules over the disk for a model with typical parameters ($M_{\rm disk} = 0.01\,M_\odot$, $M_\star = 1.0\,M_\odot$, $R_{\rm c} = 100$ au, and $\gamma = 0.8$). Despite the CO snowline being expected to be located at ~70 au, where the temperature reaches the critical value of 20 K, we see a lack of gaseous CO in the disk midplane as close as ~15 au to the star. Even within the CO snowline in a region with temperature just above 20 K, there is a constant exchange of CO molecules between gas and ice reservoirs. Here, some of the temporally frozen-out CO molecules are apparently converted into CO_2 ice before they go back to the gas. The black and gray contours in Figure 4 indicate the area, limited by the criteria outlined by Williams & Best (2014): CO is supposed to reside in the gas phase everywhere, except for the regions where it is frozen out ($T < 20$ K) or photodissociated ($\Sigma_{\rm H_2} < 1.3 \times 10^{21}\,{\rm cm}^{-2}$). But in our model, CO is not only highly depleted inside the restricted area due to chemical redistribution into other molecules, but it is also present outside of this area. Specifically, we see some CO in the outer disk region, which is shadowed from the star. In this cold region, CO is photodesorbed from dust grains, but not photodissociated by interstellar UV due to H_2 shielding. This allows CO to be present in the gas phase despite temperatures below the freezing point.

In our set of models, the average total abundance ratio iCO_2/iH_2O is 1/3. For the model shown in Figure 4, the iCO_2/iH_2O abundance ratio varies with radius from 10% to 110% in the 6–120 au range with a maximum at 20 au. CO ice dominates over CO_2 ice beyond 200 au with a maximum abundance ratio relative to water of 60% at 300 au. These characteristic abundance ratios are consistent with what is observed in most comets (Mumma & Charnley 2011). However, comparing our results to cometary abundances, one has to keep in mind that the abundances of molecules observed in comets depend also on nucleus structures and their thermal evolution (e.g., Hässig et al. 2015) and on the molecule processing in comae. The dynamical evolution of the comet ensemble is also of importance. In our model, this ratio is computed for a wide range of models and may differ from the corresponding ratios in specific models and/or spatial locations.

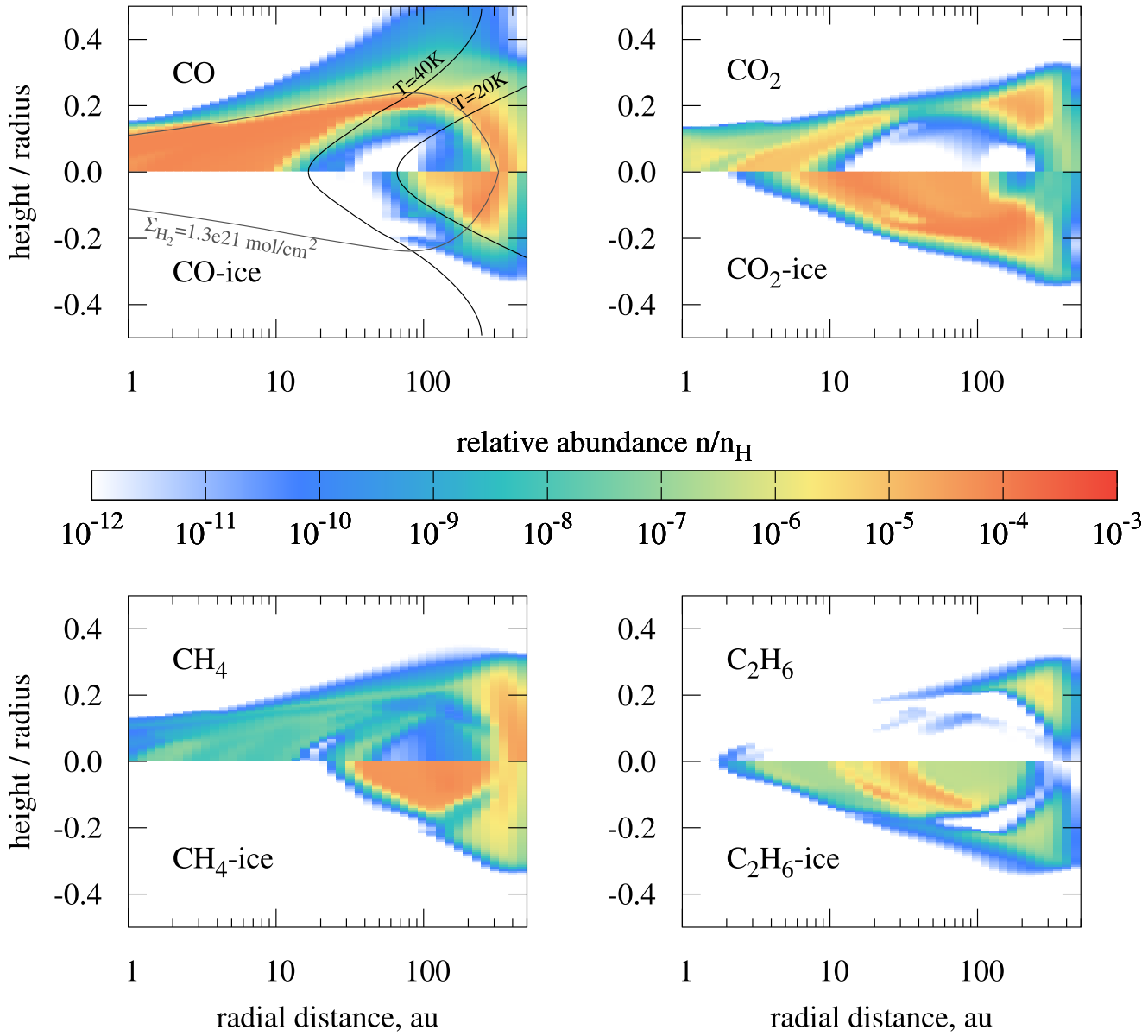

Figure 4. Abundances of major carbon-bearing species over the disk at the age of 3 Myr for one particular model ($M_{\rm disk} = 0.01\ M_\odot$, $M_\star = 1.0\ M_\odot$, $R_{\rm c} = 100$ au, and $\gamma = 0.8$). The upper half of the plots corresponds to gas abundances, while the bottom half shows the ice abundances.

The CO_2 snowline is clearly seen at ∼6 au, and a significant amount of CO_2 ice resides in the dark disk regions up to distances of about 300 au from the star. Another abundant ice, methane, has a snowline at about 20–30 au from the star and is quite abundant in the midplane from 30 to 300 au. The region of abundant ethane ice extends down to a few astronomical units to the star, while in the gas phase this molecule is nearly absent. Overall, among all of the carbon-bearing species, CO is not the most abundant, but it is the only species that does not reside mostly in ices, but in the gas phase.

Lines defined by the above criteria delineate the part of the disk that contains 56% of its mass for the presented model. In other disks from our sample, this value changes from less than 5% in extremely low-mass disks transparent to UV photons and up to 94% in warm compact disks, with the mean value of about 50% over the whole ensemble. If the ISM-like CO abundance of 10^{-4} relative to H_2 were present everywhere in the disk, and assuming that CO traces on average only 50% of the disk mass, we would get the CO-average abundance in disk equal to 5×10^{-5}. On the other hand, our chemical modeling suggests $\overline{X_{\rm CO}} = 8 \times 10^{-6}$ (see Table 3). Thus, we conclude that the CO/H_2 abundance ratio of 1.6×10^{-5} should be used to determine the disk mass from CO observations, and that qualitative criteria of CO depletion overestimate its presence in the disk by a factor of 3.

Another way to improve the Williams & Best (2014) formalism would be to apply a different value of critical temperature, below which CO is absent in the gas phase. It can be seen from Figure 4 that the abundance of CO does reach 10^{-4} in the part of the disk where it is predominantly in the gas phase. The photodissociation limit is traced as well; it only misses gaseous CO in the region of low density in the disk atmosphere far from the star, which makes an order of a few percent contribution to the total CO mass. However, the line of

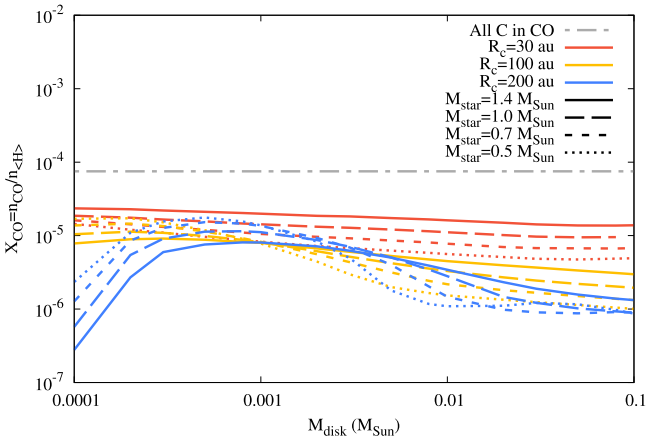

Figure 5. Total disk abundance of CO in disks of different characteristic radii R_c and around stars of different masses, $\gamma = 0.5$, at the age of 3 Myr. Line color indicates R_c, line styles (solid, dashed and dotted) indicate stellar mass. Maximum X_{CO} is shown with the gray line.

CO freeze-out defining the CO gas region should be replaced by the chemical depletion front, coincident with the $T \approx 40$ K isoline (see Figure 4).

3.3. Role of Individual Parameters

In this section, we use the grid of models to investigate how the various parameters influence the CO abundance in the disk individually. For that purpose, we fix some parameters and check how the results change due to variations in other parameters.

Figure 5 illustrates the influence of the disk radius and the stellar mass on the scatter of CO total abundance at a fixed value $\gamma = 0.5$. The star mass has only a small impact on the derived CO abundance in compact disks ($R_c = 30$ au). When we vary $M_\star$ between 0.5 and 1.4 $M_\odot$, the CO total abundance in compact disks varies only by about a factor of 3, and the higher the stellar mass, the larger the CO abundance. The influence of the stellar mass becomes more dramatic in disks of larger radii, at least, at the lower end of the considered disk mass range. Here, the same variation in $M_\star$ leads to an order of magnitude difference in X_{CO}. The overall uncertainty of the CO content reaches two orders of magnitude in the least massive disks.

It is also interesting to note that in models with lower disk masses, a hotter star leads to a smaller CO abundance, while in models with higher disk masses, the opposite trend is observed. Obviously, the CO abundance is limited by photodissociation and photodesorption, and in various situations, the higher stellar temperature can lead to either a decrease or increase in the gas-phase CO abundance. Very low-mass disks, being more transparent to stellar UV radiation, suffer from CO photodestruction, which is stronger in disks around more massive stars. Thus, these disks contain less gas-phase CO. Low-mass disks with $R_c = 30$ au do not show this trend because they encompass the same mass in a more compact region, which results in higher densities and lower influence of photodissociation. In massive disks, photodissociation is not that crucial and CO depletion is mostly caused by chemical redistribution into ices, especially CO_2 ice. A less massive star causes a CO_2 snowline closer to the star, expanding the zone where CO is effectively removed by chemical processes.

Other considered values of γ (0.8, 1.0 and 1.5) do not produce such a high variance in CO total abundance, with a larger γ giving a more stable result. The differences described above are the highest in disks with $\gamma = 0.5$, where the surface density falls off slowly, leaving more material in the outer regions of the disk, where CO depletion is stronger. The dependence on R_c is caused by a similar effect: disks of equal mass have more matter in the warm inner region if their radii are small, allowing more CO to reside in the gas phase. When R_c is large, more mass is in the cold outer area with high CO depletion.

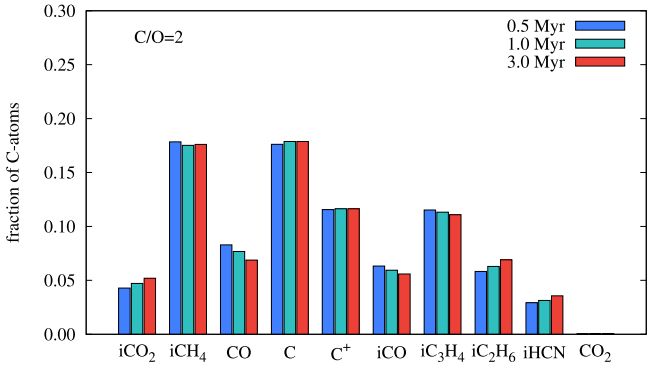

Figure 6. Same as Figure 3, but for C/O = 2.

3.4. Initial C/O Ratio

The spatial distribution of carbon described in Section 3.2 was computed for a disk with low-metals initial abundance (Table 1), where there is more oxygen than carbon ($C/O \approx 0.4$). To test the effect of other possible elemental compositions, we run 200 models, reducing the initial O abundance from 1.76×10^{-4} to 3.65×10^{-5} (leading to $C/O = 2$).

Figure 6 presents the fraction of carbon atoms locked up in the various species dominant in the disk at the previous value of C/O. Compared to Figure 3, the abundances of CO_2 and CO both in the gas and ice dropped significantly because of the lack of oxygen. On average, only ~7% of C is now in CO gas, while the amount of CO ice stays nearly the same.

Instead of CO_2 ice, we have a richer carbon chemistry on dust surfaces. In addition to ices iCH_4, iC_2H_6, and iC_3H_4, we end up with much higher abundances of molecules like iC_5H_2, iCH_3CN, iC_9H_2, iCH_3C_3N, and many other surface species with long C chains (Herbst & van Dishoeck 2009). Abundances of atomic and ionized carbon are also higher compared to the case of $C/O = 0.4$.

Overall, the carbon distribution among species and the abundance of CO depend on the initial elemental composition as well.

For the present set of models, we calculated the scatter parameter s as well. The CO scatter parameter is still close to the top with the value of 0.22; it follows N_2 with $s = 0.20$ and a few minor species having the same values of scatter but low mean abundances ($<10^{-9}$). For this elemental composition, CO_2, previously showing a low scatter, has $s = 0.60$, which worsens its applicability as a mass tracer. Among the top species, only CO and N_2 retain approximately the same values of scatter at $C/O = 2$.

4. Discussion

Although observations of molecular lines remain the only tool to determine gas masses of protoplanetary disks, their interpretation is far from being easy. Even though the most common mass

tracer in the interstellar and circumstellar medium, CO, is believed to be controlled by a relatively simple set of processes, its straightforward application to gas mass determination in protoplanetary disks has produced results, which contradict both dust observations and HD observations (Bergin et al. 2013; Favre et al. 2013; McClure et al. 2016). The discrepancy between dust-derived and CO-derived disk masses can in principle be explained by the dust evolution and gas dispersal, but it is harder to reconcile data on various molecular gas mass tracers, like CO and HD, although this difference can be reduced by accounting for the CO isotope selection and carbon underabundance in disks, as Trapman et al. (2017) suggest.

The basic assumption behind the possibility of using CO as a mass tracer is that its abundance in protoplanetary disks is defined by the balance between photodissociation and freeze-out. Williams & Best (2014) suggested a grid of models based on the assumption that CO is frozen out everywhere, where the temperature is below 20 K, and is photodissociated above the H_2 column density of $1.3 \times 10^{21}\,\mathrm{cm}^{-2}$. If none of these conditions is met, CO is assumed to have the "interstellar" abundance of 10^{-4}. It becomes increasingly clear that simple prescriptions, like the one suggested by Williams & Best (2014), can produce spurious results. First, as Williams & Best (2014) already noted, more efficient depletion pathways are possible rather than simple CO ice formation. Also, the CO sublimation temperature depends on pressure, and under conditions of the disk midplane could be higher than 20 K (Harsono et al. 2015).[6] Second, a typical "interstellar" CO abundance (inherited by the disks) can be lower than 10^{-4} (Burgh et al. 2007). One way to infer the CO/H_2 ratio in protoplanetary disks directly is to observe the absorption lines of both components in the UV band (France et al. 2014). This can be one of the prospects for future space UV missions like *WSO-Spectrum UV* (Boyarchuk et al. 2016) and *LUVOIR*.[7]

Obviously, more sophisticated methods should be used to infer the total gas mass from CO (or other molecule) observations. In a number of recent papers, the utility of CO as a mass tracer has been assessed by means of detailed models of the disk's physical and chemical structure. In a series of works by Miotello et al. (2014, 2016, 2017), a disk chemical model with isotope-selective processes was considered in order to find a way to determine the disk mass from CO isotopologue line observations. A large set of disk models was employed to study the evolution of ^{13}CO, $C^{17}O$, and $C^{18}O$ in these disks. It was concluded that CO observations can lead to gas masses being underestimated in those disks where dust grains have grown to larger sizes. Application of the results to real observations produced very low gas masses in T Tauri disks, often lower than 1 M_J. It was noted that this can be an effect of sequestering carbon atoms in more complex molecules. This option has not been considered in the above study, as the chemical model used included only a limited set of surface processes (simple hydrogenation processes). The consequence can be seen in Figure 2 from Miotello et al. (2014), where the CO depletion zone is delineated by a $T = 20$ K line and the CO snowline is located at about 100 au.

A more detailed consideration of surface processes was performed by Reboussin et al. (2015). A single surface density distribution was considered in this study, but with different vertical temperature profiles. It was shown that the surface conversion of CO into other ices, primarily CO_2 ice, leads to gas-phase CO abundances much lower than the canonical value of 10^{-4}. Abundances that high are only reached in relatively warm disks with midplane temperatures above 30 K beyond $R = 100$ au. In this work, results were presented only for the outer part of the disk ($R = 100$ and 300 au), where theoretical CO abundance can be quite sensitive to details of RT (see our results above and also observations presented in Huang et al. 2016).

A chemical evolution with a detailed account of surface reactions and carbon isotope-selective processes was considered by Yu et al. (2016, 2017). They studied the chemical evolution of a typical disk within the inner 70 au and found that due to chemical depletion, i.e., the conversion of CO into less volatile molecules, the effective CO snowline is located at about 20 au and moves toward the star as the disk evolves, even though the temperature in their model is above the CO sublimation point everywhere in the considered region. According to their results, after 3 Myr of evolution, 13.6% of all available carbon is locked in gas-phase CO, while CO_2 ice contains 36.2% of carbon atoms, which compares favorably with our results for a similar disk model (we must note that this agreement is reached despite quite different assumptions on dust properties). Although the average value of carbon partition matches well, its dispersion is significant in our modeling (from a few percent up to 50%). They also found that the CO abundance varies with time significantly, which is something that we do not see in our model. However, in their model, they vary stellar properties with time, while we keep them constant. The overall conclusion of Yu et al. (2017) is that a straightforward interpretation of CO observations leads to the underestimation of disk masses. Thus, all of the conclusions on the gas deficit in protoplanetary disks based on CO observations should be considered with caution.

The focus of the above studies was on isotope-selective processes and on the use of CO isotopologue line ratios as mass indicators. In our study, we consider CO as a whole, without distinguishing among its isotopologues, concentrating rather on the global chemical aspects of CO distributions in disks having different structural parameters.

In our study, we consider a wide range of disk sizes, masses, and surface density profiles, assuming that there is no dust evolution, so that the dust still has its interstellar parameters. Our results indicate that CO is not an ideal mass tracer, but all other molecules show greater uncertainties in the relative abundance. Still, some of them, e.g., H_2O, H_2CO, and especially CO_2, can be used as supplementary tracers, particularly if some information on the disk structure are available.

A better calibration of CO observations can be obtained using the Williams & Best (2014) method, assuming a factor of a few lower typical abundance and taking into account the chemical depletion (e.g., taking 40 K as the CO depletion temperature).

An obvious extension of the study is to consider the dependence of our results on the assumed grain size as dust is expected to grow in protoplanetary disks. Akimkin et al. (2013) have shown that the effect of grain growth at its initial stage is to shift the molecular layer closer to the dense midplane. We may provisionally expect that this is going to make molecules better gas mass tracers, but this is a subject for future study.

[6] There is also evidence for the opposite. In some cases, CO in the midplane is detected at temperatures as low as 13 K (Dartois et al. 2003), which, probably, can be explained by turbulent mixing (Semenov et al. 2006).

[7] https://asd.gsfc.nasa.gov/luvoir/

Table 4
Average Total Abundance $\overline{X_i} = 10^{\overline{xi}}$ and Scatter s_i for Ice Species

Species	$\overline{X_i}$	s_i (dex)	Species	$\overline{X_i}$	s_i (dex)	Species	$\overline{X_i}$	s_i (dex)
iSiO	8.1×10^{-10}	0.20	iCH_3CN	1.1×10^{-9}	0.62	iC_6H_6	2.1×10^{-11}	0.94
iCO_2	1.7×10^{-5}	0.26	iC_3H_4	6.7×10^{-7}	0.65	iH_2S_2	5.1×10^{-10}	0.96
iFeH	1.9×10^{-9}	0.26	iPO	1.2×10^{-11}	0.65	iH_2CO	6.6×10^{-8}	0.96
$iMgH_2$	4.4×10^{-9}	0.28	iHC_3N	2.1×10^{-11}	0.65	iH_2	1.1×10^{-7}	0.96
iC_2H_4	3.0×10^{-10}	0.28	iC_7H_2	1.9×10^{-11}	0.66	iH_2C_3O	4.6×10^{-10}	0.99
iHNC	1.1×10^{-8}	0.29	iC_8H_4	1.0×10^{-9}	0.66	iCH_3C_4H	8.0×10^{-11}	1.05
iHNCO	3.5×10^{-9}	0.34	iC_4N	1.5×10^{-11}	0.67	iNH_2CHO	2.3×10^{-9}	1.10
$iSiH_4$	3.8×10^{-9}	0.35	iH_3C_5N	3.2×10^{-11}	0.69	iCH_2CO	1.7×10^{-9}	1.17
iP	7.6×10^{-11}	0.36	iCH_3OH	5.2×10^{-8}	0.69	iHNO	3.3×10^{-9}	1.29
iHCN	9.8×10^{-7}	0.37	iC_8H_2	1.6×10^{-11}	0.70	iO_2	7.6×10^{-10}	1.32
iHCl	2.4×10^{-10}	0.38	iH_5C_3N	2.2×10^{-10}	0.71	iS_2	4.0×10^{-10}	1.38
iC_5H_2	3.3×10^{-10}	0.39	iC_7H_4	1.9×10^{-9}	0.72	iNH_2	2.3×10^{-11}	1.39
iCl	2.9×10^{-10}	0.40	iCH_4	5.3×10^{-6}	0.73	iNO	1.1×10^{-11}	1.49
iH_2O	5.1×10^{-5}	0.40	iC_5H_4	7.6×10^{-8}	0.73	iC_4H_4	4.3×10^{-10}	1.50
iNaH	9.5×10^{-10}	0.43	iC_2H_6	7.3×10^{-7}	0.74	iCH_3OCH_3	1.9×10^{-11}	1.52
iNH_3	6.6×10^{-6}	0.46	iN_2H_2	2.3×10^{-11}	0.76	iC_2H_5OH	2.0×10^{-11}	1.53
iH_2O_2	5.2×10^{-8}	0.49	iH_2CS	4.5×10^{-9}	0.81	iOH	5.0×10^{-10}	1.56
iC_3S	7.3×10^{-11}	0.49	iHCOOH	1.6×10^{-8}	0.82	iCH_3CHO	2.3×10^{-9}	1.57
iC_6H_2	9.4×10^{-11}	0.49	iC_9H_4	2.2×10^{-9}	0.83	iCH_3	3.1×10^{-11}	1.60
iNH_2OH	7.8×10^{-10}	0.53	iCH_5N	9.6×10^{-9}	0.83	iCH_2	3.0×10^{-11}	1.64
iN_2	6.8×10^{-7}	0.55	iC_9H_2	6.3×10^{-11}	0.84	iCH	2.2×10^{-11}	1.75
iCO	3.2×10^{-6}	0.58	iO_3	2.7×10^{-9}	0.85	iO	1.3×10^{-10}	1.75
iH_2S	2.3×10^{-8}	0.59	iHS_2	2.3×10^{-10}	0.86	iC	2.2×10^{-11}	1.86
iC_3H_2	1.2×10^{-9}	0.60	iC_6H_4	1.8×10^{-8}	0.88	iH	2.4×10^{-9}	1.98
iC_2H_2	9.5×10^{-11}	0.61	iN_2O	1.1×10^{-11}	0.92			

5. Conclusions

We conducted a chemical modeling of ~1000 protoplanetary disk structures around low-mass stars with different parameters to find out species that have the best correlation with the total disk mass. We varied the central star mass, the disk characteristic radius, the disk mass, and the γ index of the surface density distribution, assuming MRN grain size distribution for the UV RT in the disk atmosphere and 0.1 μm size grains for the surface chemistry. The chemical modeling is based on the updated non-equilibrium chemical network ALCHEMIC (Semenov & Wiebe 2011) incorporated into the ANDES code (Akimkin et al. 2013). We focused on an intrinsic dispersion of species abundance due to unknown structural and thermal parameters. The main conclusions are:

1. Among all 650 considered species, the relative abundance of the CO molecule has one of the smallest scatters in the overall disk ensemble (with the obvious exceptions of hydrogen and helium). The characteristic reference "1σ" values for the logarithm of the species total disk abundance at an age of 3 Myr are 0.28 dex for CO and CO_2, 0.29 dex for H_2CO, and 0.51 dex for H_2O (see Table 3 for other species). So, even in the case of CO, there is a maximum uncertainty of one order of magnitude in CO abundance if the disk physical structure is unknown. More reliable CO disk masses can be obtained if the disk characteristic radius R_c is determined.

2. On average, in the whole disk ensemble, ≈13% of carbon atoms end up in the gas-phase CO molecule (for the initial "low-metals" abundance from Lee et al. 1998 where C/O = 0.4). The average value of carbon partitioning is in good agreement with the conclusions by Yu et al. (2016). However, the extreme values vary from ≈2% for large and massive disks to ≈30% for compact disks with small and moderate masses. Statistically, the most abundant carbon-bearing species is CO_2 ice, with an average C atom fraction of ≈25%. The majority of the remaining carbon atoms are in CH_4 and CO ices (17% and 7% of C atoms, respectively), C and C^+ (14% and 8%), and ices of complex organic species. The degree of carbon atom redistribution into non-CO molecules is naturally more effective if C/O >1. Quantitatively, the average carbon partition into CO is 7% for C/O = 2.

3. Despite CO having a noticeable variance in the relative abundance, it is still the best molecular tracer of disk gas mass. The typical value of the total CO/H_2 abundance ratio is 1.6×10^{-5} with "1σ" limits from 0.8×10^{-5} to 3.0×10^{-5}. CO_2 also has a low abundance variance, although this variance depends strongly on the C/O ratio. Other species that have relatively good correlation with disk mass are H_2O and H_2CO.

We find that on average the total abundance of gaseous CO in protoplanetary disks is ≈6 times lower compared to the interstellar value of 10^{-4}. Chemical depletion lowers the abundance of CO by a factor of 3, compared to the case of photodissociation and freeze-out as the only ways of CO destruction.

We thank the referee for fruitful comments that helped us improve our model and formulate better conclusions. T.M., V.A., and D.W. acknowledge financial support from the Russian Science Foundation (17-12-01441; Sections 2, 3, 5). D.S. acknowledges support from the Heidelberg Institute of Theoretical Studies for the project "Chemical kinetics models and visualization tools: Bridging biology and astronomy." A.V. acknowledges support from the European Research Council (ERC; project PALs 320620).

Appendix
Ice Species

Here we present a version of Table 3 for ice species. Table 4 lists ice species with average total abundance in the disk above 10^{-11} sorted by scatter.

ORCID iDs

Tamara Molyarova https://orcid.org/0000-0003-0448-6354
Vitaly Akimkin https://orcid.org/0000-0002-4324-3809
Anton Vasyunin https://orcid.org/0000-0003-1684-3355
Dmitri Wiebe https://orcid.org/0000-0002-5111-0395

References

Akimkin, V., Zhukovska, S., Wiebe, D., et al. 2013, ApJ, 766, 8
Akimkin, V. V. 2015, ARep, 59, 747
Andrews, S. M., & Williams, J. P. 2005, ApJ, 631, 1134
Ansdell, M., Williams, J. P., Manara, C. F., et al. 2017, AJ, 153, 240
Ansdell, M., Williams, J. P., van der Marel, N., et al. 2016, ApJ, 828, 46
Armitage, P. J. 2015, arXiv:1509.06382
Bai, X.-N., & Goodman, J. 2009, ApJ, 701, 737
Baraffe, I., Homeier, D., Allard, F., & Chabrier, G. 2015, A&A, 577, A42
Bergin, E. A., Cleeves, L. I., Gorti, U., et al. 2013, Natur, 493, 644
Bergin, E. A., Hogerheijde, M. R., Brinch, C., et al. 2010, A&A, 521, L33
Bitsch, B., Lambrechts, M., & Johansen, A. 2015, A&A, 582, A112
Bohlin, R. C., Savage, B. D., & Drake, J. F. 1978, ApJ, 224, 132
Bolatto, A. D., Wolfire, M., & Leroy, A. K. 2013, ARA&A, 51, 207
Boyarchuk, A. A., Shustov, B. M., Savanov, I. S., et al. 2016, ARep, 60, 1
Burgh, E. B., France, K., & McCandliss, S. R. 2007, ApJ, 658, 446
Carmona, A., van der Plas, G., van den Ancker, M. E., et al. 2011, A&A, 533, A39
Chapillon, E., Guilloteau, S., Dutrey, A., Piétu, V., & Guélin, M. 2012, A&A, 537, A60
Chapillon, E., Parise, B., Guilloteau, S., & Du, F. 2011, A&A, 533, A143
Chiang, E. I., & Goldreich, P. 1997, ApJ, 490, 368
Dartois, E., Dutrey, A., & Guilloteau, S. 2003, A&A, 399, 773
Draine, B. T. 2006, ApJ, 636, 1114
Dullemond, C. P., & Dominik, C. 2004, A&A, 421, 1075
Dullemond, C. P., Dominik, C., & Natta, A. 2001, ApJ, 560, 957
Dunham, M. M., Vorobyov, E. I., & Arce, H. G. 2014, MNRAS, 444, 887
Dutrey, A., Guilloteau, S., & Guelin, M. 1997, A&A, 317, L55
Dutrey, A., Wakelam, V., Boehler, Y., et al. 2011, A&A, 535, A104
Favre, C., Cleeves, L. I., Bergin, E. A., Qi, C., & Blake, G. A. 2013, ApJL, 776, L38
France, K., Herczeg, G. J., McJunkin, M., & Penton, S. V. 2014, ApJ, 794, 160
Goldsmith, P. F., Bergin, E. A., & Lis, D. C. 1997, ApJ, 491, 615
Guilloteau, S., Reboussin, L., Dutrey, A., et al. 2016, A&A, 592, A124
Harsono, D., Bruderer, S., & van Dishoeck, E. F. 2015, A&A, 582, A41
Hartmann, L., Calvet, N., Gullbring, E., & D'Alessio, P. 1998, ApJ, 495, 385
Hässig, M., Altwegg, K., Balsiger, H., et al. 2015, Sci, 347, aaa0276
Henning, T., & Meeus, G. 2011, in Dust Processing and Mineralogy in Protoplanetary Accretion Disks, ed. P. J. V. Garcia (Chicago, IL: Univ. Chicago Press), 114
Henning, T., & Semenov, D. 2008, in IAU Symp. 251, Organic Matter in Space, ed. S. Kwok & S. Sanford (Cambridge: Cambridge Univ. Press), 89
Henning, T., & Semenov, D. 2013, ChRv, 113, 9016
Herbst, E., & van Dishoeck, E. F. 2009, ARA&A, 47, 427
Hogerheijde, M. R., Bergin, E. A., Brinch, C., et al. 2011, Sci, 334, 338
Huang, J., Öberg, K. I., & Andrews, S. M. 2016, ApJL, 823, L18
Isella, A., Guidi, G., Testi, L., et al. 2016, PhRvL, 117, 251101
Ivlev, A. V., Akimkin, V. V., & Caselli, P. 2016, ApJ, 833, 92
Laor, A., & Draine, B. T. 1993, ApJ, 402, 441
Lee, H.-H., Roueff, E., Pineau des Forets, G., et al. 1998, A&A, 334, 1047
Loomis, R. A., Cleeves, L. I., Öberg, K. I., Guzman, V. V., & Andrews, S. M. 2015, ApJL, 809, L25
Mathis, J. S., Mezger, P. G., & Panagia, N. 1983, A&A, 128, 212
Mathis, J. S., Rumpl, W., & Nordsieck, K. H. 1977, ApJ, 217, 425
McClure, M. K., Bergin, E. A., Cleeves, L. I., et al. 2016, ApJ, 831, 167
Miotello, A., Bruderer, S., & van Dishoeck, E. F. 2014, A&A, 572, A96
Miotello, A., van Dishoeck, E. F., Kama, M., & Bruderer, S. 2016, A&A, 594, A85
Miotello, A., van Dishoeck, E. F., Williams, J. P., et al. 2017, A&A, 599, A113
Mordasini, C., Alibert, Y., Benz, W., Klahr, H., & Henning, T. 2012, A&A, 541, A97
Mumma, M. J., & Charnley, S. B. 2011, ARA&A, 49, 471
Öberg, K. I., Guzmán, V. V., Furuya, K., et al. 2015, Natur, 520, 198
Öberg, K. I., Guzmán, V. V., Merchantz, C. J., et al. 2017, ApJ, 839, 43
Okuzumi, S. 2009, ApJ, 698, 1122
Qi, C., D'Alessio, P., Öberg, K. I., et al. 2011, ApJ, 740, 84
Qi, C., Öberg, K. I., & Wilner, D. J. 2013, ApJ, 765, 34
Rab, C., Elbakyan, V., Vorobyov, E., et al. 2017, A&A, 604, A15
Reboussin, L., Wakelam, V., Guilloteau, S., Hersant, F., & Dutrey, A. 2015, A&A, 579, A82
Salinas, V. N., Hogerheijde, M. R., Bergin, E. A., et al. 2016, A&A, 591, A122
Sano, T., Miyama, S. M., Umebayashi, T., & Nakano, T. 2000, ApJ, 543, 486
Semenov, D., & Wiebe, D. 2011, ApJS, 196, 25
Semenov, D., Wiebe, D., & Henning, T. 2006, ApJL, 647, L57
Thi, W.-F., Ménard, F., Meeus, G., et al. 2011, A&A, 530, L2
Trapman, L., Miotello, A., Kama, M., van Dishoeck, E. F., & Bruderer, S. 2017, A&A, 605, A69
Tsukamoto, Y., Okuzumi, S., & Kataoka, A. 2017, ApJ, 838, 151
Vasyunin, A. I., Caselli, P., Dulieu, F., & Jiménez-Serra, I. 2017, ApJ, 842, 33
Vasyunina, T., Vasyunin, A. I., Herbst, E., & Linz, H. 2012, ApJ, 751, 105
Wakelam, V., Loison, J.-C., Herbst, E., et al. 2015, ApJS, 217, 20
Walsh, C., Loomis, R. A., Öberg, K. I., et al. 2016, ApJL, 823, L10
Williams, J. P., & Best, W. M. J. 2014, ApJ, 788, 59
Williams, J. P., & Cieza, L. A. 2011, ARA&A, 49, 67
Williams, J. P., & McPartland, C. 2016, ApJ, 830, 32
Yu, M., Evans, N. J., II, Dodson-Robinson, S. E., Willacy, K., & Turner, N. J. 2017, ApJ, 841, 39
Yu, M., Willacy, K., Dodson-Robinson, S. E., Turner, N. J., & Evans, N. J., II 2016, ApJ, 822, 53
Zhang, K., Bergin, E. A., Blake, G. A., Cleeves, L. I., & Schwarz, K. R. 2017, NatAs, 1, 0130